JOURNAL OF SYNCHROTRON RADIATION
ISSN 1600-5775

Thorium(IV) adsorption onto multilayered $Ti_3C_2T_x$ MXene: a batch, X-ray diffraction and EXAFS combined study

Lin Wang,[a]‡ Wuqing Tao,[b,c]‡ Enzhao Ma,[a] Zijie Li,[a] Peng Ren,[a] Yujuan Zhang,[d] Zhirong Liu,[b]* Liyong Yuan[a]* and Weiqun Shi[a]

[a]Laboratory of Nuclear Energy Chemistry, Institute of High Energy Physics, Chinese Academy of Sciences, Beijing 100049, People's Republic of China, [b]School of Chemistry, Biological and Materials Science, East China University of Technology, Nanchang 330013, People's Republic of China, [c]College of Science, Jiangxi Agricultural University, Nanchang 330045, People's Republic of China, and [d]School of Materials Science and Engineering, University of Science and Technology Beijing, Beijing 100083, People's Republic of China. *Correspondence e-mail: 199760011@ecut.edu.cn, yuanly@ihep.ac.cn

Received 7 September 2021
Accepted 14 October 2021

Edited by S. Butorin, Uppsala University, Sweden

‡ These authors contributed equally to this work.

Keywords: MXene; actinide; adsorption mechanism; EXAFS.

Supporting information: this article has supporting information at journals.iucr.org/s

The interlayer regulation of layered environmental adsorption materials such as two-dimensional early transition metal carbides and carbonitrides (MXenes) plays an important role in their purification performance for specific pollutants. Here the enhanced uptake of Th^{IV} by multilayered titanium carbides ($Ti_3C_2T_x$) through a hydrated intercalation strategy is reported. Th^{IV} adsorption behaviors of three $Ti_3C_2T_x$ samples with different *c* lattice parameters were studied as a function of contact time, pH, initial concentration, temperature and ion strength in batch experiments. The results indicated that the Th^{IV} uptake was pH and ionic strength dependent, and the adsorption process followed the pseudo-second-order kinetics and the heterogeneous isotherm (Freundlich) model. Thermodynamic data suggested that the adsorption process of all MXene samples was a spontaneous endothermic reaction. The dimethyl sulfoxide intercalated hydrated $Ti_3C_2T_x$ featured the largest interlayer space and exhibited the highest Th^{IV} adsorption capacity (162 mg g^{-1} at pH 3.4 or 112 mg g^{-1} at pH 3.0), reflecting the significant increase in available adsorption sites from $Ti_3C_2T_x$ interlayers. The adsorption mechanism has been clarified based on adsorption experiments and spectroscopic characterizations. An ion exchange process was proposed for the interaction between hydrated MXenes and Th^{IV}, where H^+ from surface $[Ti{-}O]^-H^+$ groups were the primary active sites on $Ti_3C_2T_x$. Extended X-ray absorption fine structure (EXAFS) fitting results, in combination with X-ray diffraction (XRD) and Fourier transform infrared spectroscopy (FTIR) analyses, clearly indicated that Th^{IV} mainly formed the outer-sphere complexes on $Ti_3C_2T_x$ surface through electrostatic interaction under strong acid conditions, while at pH > 3.0 the adsorption mechanism was determined by inner-sphere coordination and electrostatic interaction together.

1. Introduction

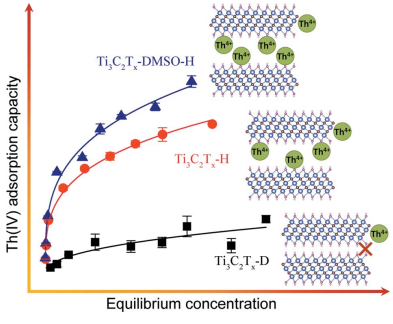

As a long-lived natural radioactive element, thorium is a potential nuclear fuel for the next-generation reactors (*e.g.* liquid fluoride thorium reactor) with advantages of large abundance, low cost, low risk of nuclear proliferation and almost no waste (Wang, Brown *et al.*, 2018; Wang, Liu *et al.*, 2018). In addition to the nuclear industry, thorium and its compounds are widely used in the applications of efficient catalysis, refractory materials, high-quality lenses and aviation alloy manufacturing (Rao *et al.*, 2006). In terms of environmental concerns, a significant amount of thorium-containing waste has been discharged by ore processing in the rare earth industry, coal burning in thermal power plants and the use of

chemical fertilizers. The radioactive nature and heavy metal toxicity of thorium may lead to great hazards for public health and ecosystems (Zhou *et al.*, 2021). In aqueous solutions, thorium usually exists in the form of stable Th^{IV}, which can be deposited in bone, kidney and liver (Liu *et al.*, 2019; Rao *et al.*, 2006), thus causing permanent damage to the human body. In addition, Th^{IV} is often used as a chemical analog of other tetravalent actinides to simulate their migration and transformation behavior in the environment (Chen & Wang, 2007). The development of novel materials featuring high uptake capacity, good stability and excellent selectivity for Th^{IV} capture is urgently desired with regard to the effective utilization of thorium resources and radioactive pollution remediation.

Because of the large pre-concentration coefficient and facile operation, adsorption is one of the most attractive approaches for thorium extraction from aqueous solution. In the past few decades, a large number of solid-phase adsorbents such as metal oxide particles (Reiller *et al.*, 2005; Rojo *et al.*, 2009; Tan *et al.*, 2007; Yusan *et al.*, 2016), inorganic porous materials (Alahabadi *et al.*, 2020; Sheng *et al.*, 2008; Misaelides *et al.*, 1995), functionalized mesoporous silica (Lebed *et al.*, 2011; Yuan *et al.*, 2014; Zhang, Ma *et al.*, 2020), polymers (Yuan *et al.*, 2019), organic–inorganic hybrids (Abbasizadeh *et al.*, 2013; Kaygun & Akyil, 2007) and metal–organic framework (MOF) materials (Moghaddam *et al.*, 2018; Zhang *et al.*, 2017) have been widely examined to evaluate Th^{IV} separation from artificial and/or environmental wastewater. Apart from the above materials, the layered adsorbents provide numerous surface atoms and have unique structures with intralayer covalent bonding and interlayer van der Waals bonding (Wang *et al.*, 2020), which allow the facile regulation of surface and interlayer properties to prepare multifunctional adsorbents for Th^{IV} elimination. Compared with the natural layered minerals (*e.g.* phlogopite, bentonite, illite and sepiolite) (Erden & Donat, 2017; Fralova *et al.*, 2021; Wu *et al.*, 2018; Zhang *et al.*, 2016; Zhao, 2008), the emerging two-dimensional materials such as graphene oxide (Bai *et al.*, 2014; Li, Yang *et al.*, 2018) and layered sulfides (Li, Li *et al.*, 2018; Xu *et al.*, 2021) exhibit much higher thorium removal capacity and better selectivity under acidic conditions, which reflects the great potential of novel lamellar materials in radionuclide remediation.

Two-dimensional transition metal carbides and carbonitrides (MXenes) are a family of layered materials with hexagonal structure and the general chemical formula of $M_{n+1}X_nT_x$ discovered in the past decade, where M represents an early transition metal, X represents C and/or N, T_x denotes surface termination groups, and n = 1–3 (Naguib *et al.*, 2011, 2012). So far, MXene has been widely used in the application fields of catalysis, energy storage, sensing and environment (VahidMohammadi *et al.*, 2021; Li *et al.*, 2019), and the specific performance of this material largely depends on its chemical bonding and surface termination properties (Magnuson & Näslund, 2020; Naslund *et al.*, 2021). Benefiting from the variable element composition, abundant oxygen-containing surface groups and good hydrophilicity, MXenes have proved to be promising environmental remediation materials in the field of water purification (Rasool *et al.*, 2019; Ihsanullah, 2020; Chen *et al.*, 2020). In terms of radionuclide elimination, various MXenes (*e.g.* $Ti_3C_2T_x$, V_2CT_x, T_2CT_x) and their composites and derivatives have been synthesized to investigate the corresponding adsorption behavior for Cs^{I} (Jun, Jang *et al.*, 2020; Khan *et al.*, 2019; Shahzad *et al.*, 2020), Sr^{II} (Jun, Park *et al.*, 2020), Ba^{II} (Mu *et al.*, 2018), Pd^{II} (Mu *et al.*, 2019), Eu^{III} (Zhang, Wang *et al.*, 2020), U^{VI} (Wang, Song *et al.*, 2018; Wang *et al.*, 2016, 2021), Re^{VII}/Tc^{VII} (Wang *et al.*, 2019) and I^- (Huang *et al.*, 2020). For Th^{IV}, only one preliminary study has reported its adsorption on Ti_2CT_x MXene (Li *et al.*, 2019), and results indicated that the adsorption had a high distribution coefficient and was independent of ionic strength. However, the easily degradable nature of Ti_2CT_x in environmental atmosphere and water greatly limits its environmental application. Moreover, the rational utilization of the spontaneous intercalation behavior of MXenes is of great importance, because the uptake performance may be significantly improved by weakening the interlayer interaction of multilayer structures. Herein, we report the adsorption of Th^{IV} on more stable $Ti_3C_2T_x$ MXene as extended research. The effect of interlayer regulation of $Ti_3C_2T_x$ on the adsorption behavior has been examined in detail by batch experiments. Furthermore, the underlying adsorption mechanism is also deciphered by EXAFS (extended X-ray absorption fine structure), XRD (X-ray diffraction) and FTIR (Fourier transform infrared) spectroscopy analyses.

2. Experimental

2.1. Reagents

All the chemicals used as-received in this study were analytical grade and obtained from Sinopharm Chemical Reagent Co. Ltd. A 10 g l^{-1} thorium stock solution was prepared by dissolving an appropriate amount of thorium nitrate pentahydrate [$Th(NO_3)_4{\cdot}5H_2O$] in deionized water acidified with nitric acid.

2.2. Preparation of $Ti_3C_2T_x$ MXenes

The pristine and intercalated $Ti_3C_2T_x$ samples were synthesized according to the literature (Wang *et al.*, 2017). Briefly, a pristine $Ti_3C_2T_x$ water suspension ($Ti_3C_2T_x$-H) was prepared by etching Ti_3AlC_2 with 15 wt% HF and washing with deionized water. Dry $Ti_3C_2T_x$ sample (labeled as $Ti_3C_2T_x$-D) was obtained by filtering and vacuum drying $Ti_3C_2T_x$-H MXene at room temperature. The filtered $Ti_3C_2T_x$-H was dispersed in dimethyl sulfoxide (DMSO) for 2 days, and then washed with deionized water to prepare a water suspension of hydrated DMSO-intercalated $Ti_3C_2T_x$ (labeled as $Ti_3C_2T_x$-DMSO-H). To avoid the slow oxidation, $Ti_3C_2T_x$-H and $Ti_3C_2T_x$-DMSO-H were stored in polypropylene bottles filled with Ar at 277 K (4°C) for later use. The mass concentrations of hydrated samples were measured by calculating the weight of MXene after filtering and drying the suspension with a fixed volume.

2.3. Batch adsorption experiments

A series of adsorption experiments for Th^{IV} uptake in aqueous solution by various $Ti_3C_2T_x$ samples were performed as a function of contact time, pH, initial Th^{IV} concentration (C_0), temperature, ionic strength and other competing metal cations. The Th^{IV} stock solution was diluted to initial concentrations ranging from 5 to 150 mg l^{-1} to carry out adsorption experiments by a batch method. Typically, 4 mg MXene was mixed with an appropriate amount of deionized water to keep the total volume of suspension as 5 ml in a beaker. Then 5 ml of solution containing Th^{IV} or multi-metal ions was added such that the concentration of sorbent was 0.4 g l^{-1}. The pH value of the solution was adjusted with small amounts of 0.1 *M* NaOH and 0.1 *M* HNO_3, and then the solution was stirred at room temperature for a specified time. The solid adsorbent was removed after Th^{IV} adsorption to obtain the supernatant sample by using a polyethersulfone syringe filter (0.22 µm, ANPEL Scientific Instrument Co. Ltd, Shanghai). The supernatant was diluted with 5 wt% HNO_3 before the final concentration determination. For the ionic strength experiment, $NaClO_4$ (0.1–500 mmol l^{-1}) was selected as representative electrolytes. In the selective adsorption test, all initial concentrations of Th^{IV} and other competing metal ions, including Co^{2+}, Ni^{2+}, Zn^{2+}, Sr^{2+}, La^{3+}, Nd^{3+}, Sm^{3+}, Gd^{3+} and Yb^{3+}, were 0.5 mmol l^{-1}. The residual concentrations of thorium and other metal elements were determined by an inductively coupled plasma optical emission spectrograph (ICP-OES, Horiba JY2000-2, France).

For the above batch adsorption experiments, the uptake capacity Q_e (mg g^{-1}) and distribution coefficient K_d (ml g^{-1}) were calculated using the following equations:

$$Q_e = (C_0 - C_e)\,V/m \quad (1)$$

$$K_d = (C_0 - C_e)\,V/mC_e \quad (2)$$

where C_0 and C_e are the initial and final equilibrium concentration of cations, respectively, and V and m are the volume of solution and the mass amount of solid sorbent in the batch adsorption tests, respectively. All the adsorption experiments have been carried out at least twice, and the uncertainty of measurement is less than 5%.

2.4. Material characterization

The morphologies and chemical compositions of the MXene samples were analyzed by a Hitachi S-4800 field-emission scanning electron microscope equipped with Horiba 7593-H energy-dispersive X-ray spectroscopy (EDS). A Bruker D8 Advance diffractometer (Cu $K\alpha$ radiation, λ = 1.5406 Å) was used to collect powder XRD patterns. The step size for XRD pattern scanning was 0.02°. A Bruker Tensor 27 spectrometer was used to measure the FTIR spectra of samples by a potassium bromide pellet method.

The L_3 edge (16300 eV) EXAFS spectra of Th were collected at beamline 1W1B of the Beijing Synchrotron Radiation Facility (BSRF) using a silicon (111) double-crystal monochromator. $Th(NO_3)_4{\cdot}5H_2O$ (reference) was measured in transmission mode while other samples were measured in fluorescence mode using a Lytle-type ion chamber detector. EXAFS oscillation data were extracted, analyzed and fitted using computer programs *Athena* and *Artemis*, which were parts of the *IFEFFIT* program package (Ravel & Newville, 2005). A k range of ~1.8−11.5 $Å^{-1}$ and a background frequency cutoff parameter (Rbkg) of 1.2 were used for acquisition of the Fourier transform of k^3-weighted EXAFS data. To fit parameters such as coordination number (CN), atomic distance (R) and Debye–Waller factor (σ^2), the theoretical phase and amplitude functions for the scattering pathways of Th–O and Th–N were calculated based on the crystal structures of $Th(NO_3)_4{\cdot}5H_2O$. The fitting procedures were carried out in R space from 1.2 to 3.5 Å for $Th(NO_3)_4{\cdot}5H_2O$ and 1.2 to 3.0 Å for other samples with a fixed amplitude reduction factor (S_0^2) of 0.97.

3. Results and discussion

3.1. Characterization

MXene samples of $Ti_3C_2T_x$-D, $Ti_3C_2T_x$-H and $Ti_3C_2T_x$-DMSO-H were prepared by drying, wetting and intercalating multilayered $Ti_3C_2T_x$. Their powder XRD patterns are shown in Fig. 1. The (002) peak of $Ti_3C_2T_x$-D is centered at 2θ of 8.8°, corresponding to a c lattice parameter (c-LP) of 20.0 Å. Because of the hydration effect and co-intercalation of H_2O/DMSO molecules inside the MXene interlayer, the (002) peak position shifts to 6.8° and 4.6° for $Ti_3C_2T_x$-H and $Ti_3C_2T_x$-DMSO-H, respectively, which results in much larger c-LPs (25.9 and 38.1 Å). Furthermore, the good reproducibility of intercalated MXene preparation has been proved using $Ti_3C_2T_x$-DMSO-H as a demonstration (Fig. S1 in the supporting information). The SEM (scanning electron microscopy) images in Fig. 2 indicate that $Ti_3C_2T_x$-D, $Ti_3C_2T_x$-H and $Ti_3C_2T_x$-DMSO-H have similar morphology, *i.e.* they feature micrometre-sized bulk particles composed of nano-lamellar structures. The above results are in good agreement with our previous study (Wang *et al.*, 2017).

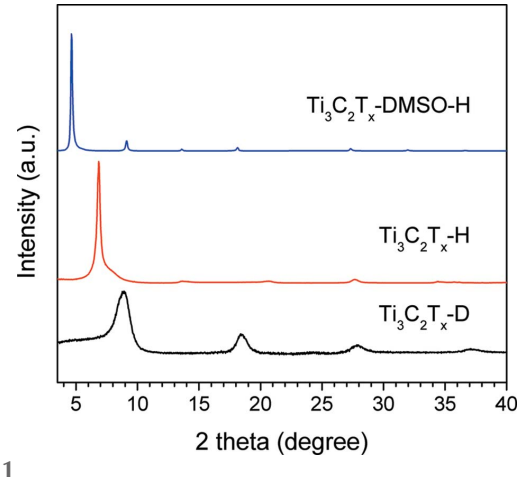

Figure 1
XRD patterns of the pristine dry, hydrated and DMSO-intercalated $Ti_3C_2T_x$.

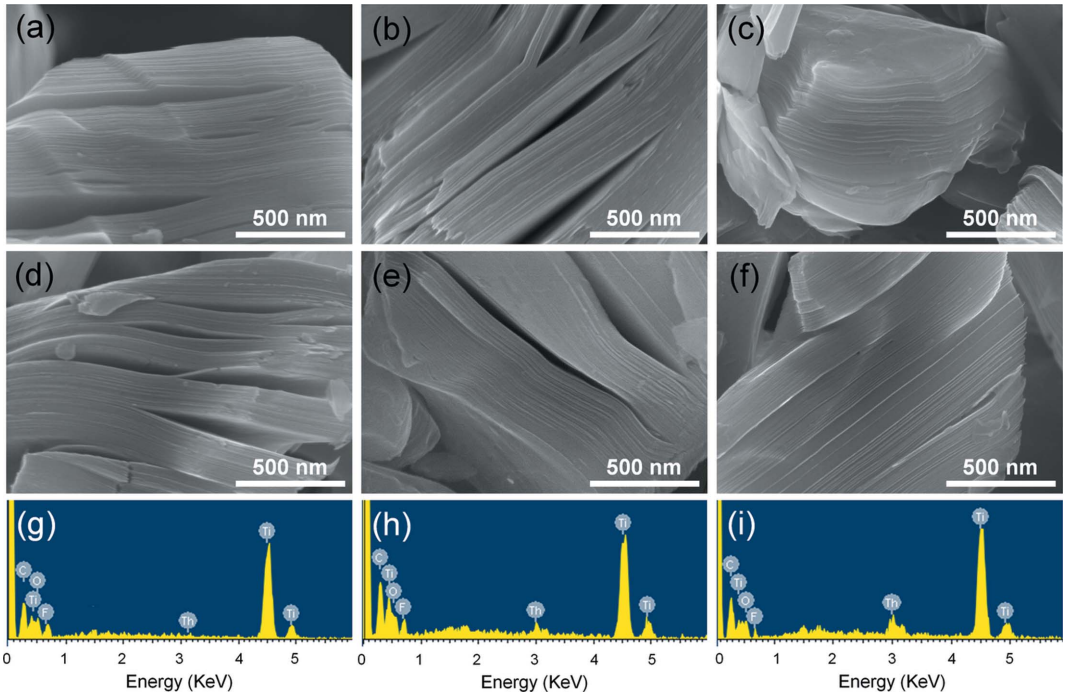

Figure 2
SEM images and EDS results of different MXene samples before (*a*)–(*c*) and after (*d*)–(*i*) Th^{IV} adsorption. (*a*), (*d*), (*g*) $Ti_3C_2T_x$-D; (*b*), (*e*), (*h*) $Ti_3C_2T_x$-H; (*c*), (*f*), (*i*) $Ti_3C_2T_x$-DMSO-H.

3.2. Adsorption kinetics

The adsorption kinetics experiments of radioactive Th^{IV} onto the three MXene samples were carried out at a concentration of 100 mg l^{-1} and pH 3.4, with the results shown in Fig. 3(*a*). The adsorption of Th^{IV} on $Ti_3C_2T_x$-D reached a plateau in 30 min with an uptake capacity of 37 mg g^{-1}. The hydrated and intercalated MXenes showed much higher Th^{IV} removal performance but slower kinetics, and the equilibration times for $Ti_3C_2T_x$-H and $Ti_3C_2T_x$-DMSO-H were 90 and 300 min, respectively. Previous literature (Wang *et al.*, 2017) and XRD measurements in this study (see below, Section 3.7) have demonstrated that the adsorption of cations by dry MXene sample mainly occurs on the external surface because its interlayer space is too narrow, while the hydrated and intercalated MXene could provide a large amount of interlayer adsorption sites besides the exterior surface adsorption sites; therefore $Ti_3C_2T_x$-H and $Ti_3C_2T_x$-DMSO-H exhibited much larger Th^{IV} uptake capacities than $Ti_3C_2T_x$-D in this work. Our results suggest that the adsorption of Th^{IV} inside MXene interlayers corresponds to a slower internal diffusion process; this is because the 'deep' adsorption sites in multilayer MXene particles may require sufficient diffusion of Th^{IV} in the confinement space.

In order to clarify the adsorption process, the pseudo-second-order kinetic model was used to analyze the experi-

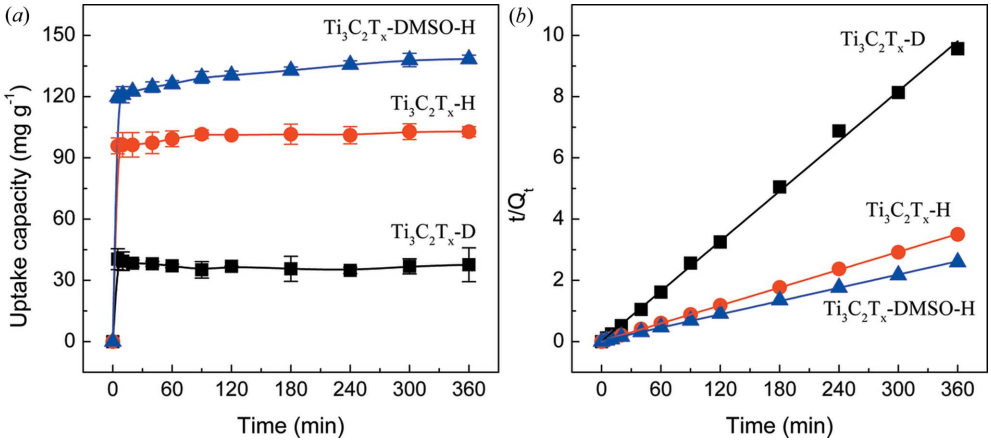

Figure 3
Th^{IV} adsorption kinetics of MXene samples and linear fitting data with the pseudo-second-order kinetic model. (C_0 = 100 mg l^{-1}, m/V = 0.4 g l^{-1}, pH = 3.4 ± 0.1.)

Table 1
Kinetics model parameters and correlation coefficients for Th^{IV} adsorption on $Ti_3C_2T_x$-D, $Ti_3C_2T_x$-H and $Ti_3C_2T_x$-DMSO-H.

	Pseudo-second-order model			Equilibrium capacity (mg g^{-1})
	Q_e (mg g^{-1})	k (g mg^{-1} min^{-1})	R^2	
$Ti_3C_2T_x$-D	37	0.0368	0.998	37
$Ti_3C_2T_x$-H	103	0.0074	0.999	102
$Ti_3C_2T_x$-DMSO-H	138	0.0020	0.999	138

mentally observed kinetic data and the linear fitting results are shown in Fig. 3(*b*). The linearized form of the model is given as follows:

$$t/Q_t = 1/kQ_e^2 + t/Q_e \quad (3)$$

where Q_e (mg g^{-1}) and Q_t (mg g^{-1}) are the quantities of the sorbed Th^{IV} at equilibrium time and time t, respectively, and k (g mg^{-1} min^{-1}) is the pseudo-second-order adsorption rate constant. The model parameters and correlation coefficients obtained by the model are listed in Table 1.

It can be clearly seen that t/Q_t has a good linear relationship with t for the adsorption kinetics of all three MXene samples, and the correlation coefficients (R^2) are close to 1. Additionally, the calculated removal capacities of $Ti_3C_2T_x$-D, $Ti_3C_2T_x$-H and $Ti_3C_2T_x$-DMSO-H based on the model are similar to the experimental equilibrium capacities (Table 1). The pseudo-second-order kinetic model describes the removal of Th^{IV} on $Ti_3C_2T_x$ MXenes quite well, revealing that the kinetics are determined by two components which may be related to the diffusion of Th^{IV} and the occupation of adsorption sites on MXene surface.

3.3. Effect of pH

Fig. 4 represents the removal of Th^{IV} by $Ti_3C_2T_x$-D, $Ti_3C_2T_x$-H and $Ti_3C_2T_x$-DMSO-H as a function of pH. The uptake of Th^{IV} for the three MXene samples shows an overall increasing trend with the increase in solution pH, which is ascribed to the changes in the surface charge of MXene and the species of Th^{IV} in the solutions. Since pristine $Ti_3C_2T_x$ and its intercalated products had similar zero charge points around pH 2.0–2.5 (Ying *et al.*, 2015), their surfaces were positively charged under very acidic conditions. In this case, the adsorption of cationic Th^{IV} on $Ti_3C_2T_x$ MXenes was greatly inhibited due to the electrostatic repulsion and the competition of the high concentration of H^+. Nonetheless, $Ti_3C_2T_x$-DMSO-H still exhibited a considerable adsorption capacity (~45 mg g^{-1}) at pH 1.5, implying that its largest interlayer space promotes the ion exchange of protons on the MXene surface (in the form of $[Ti–O]^-H^+$) with Th^{IV}. As the pH increased above 2.5, the surface of $Ti_3C_2T_x$ became negatively charged, and the electrostatic interaction between adsorbent and Th^{IV} resulted in an increase in adsorption capacity. The species distribution of Th^{IV} as a function of pH was calculated using the *Medusa/Hydra* software. It can be seen from Fig. S2 that although there is no $Th(OH)_4$ precipitation under the experimental conditions, the partial hydrolysis species of Th^{IV} including $Th(OH)^{3+}$ and $Th(OH)_2^{2+}$ formed with the increase in pH. The fractions of $Th(OH)^{3+}$ and $Th(OH)_2^{2+}$ increase sharply at pH > 2.0 and pH > 3.0, respectively, which also contributes to the increase of Th^{IV} adsorption capacity at high pH conditions.

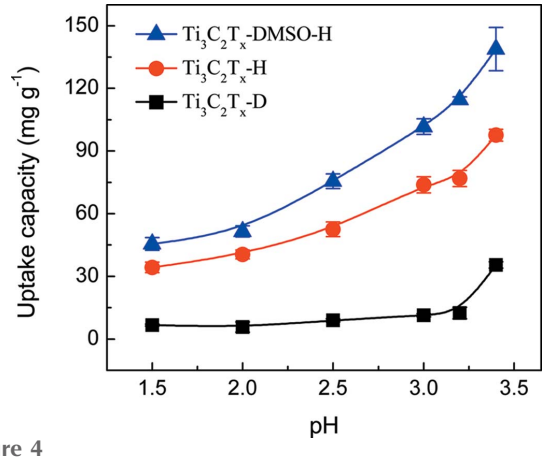

Figure 4
Th^{IV} adsorption by $Ti_3C_2T_x$-D, $Ti_3C_2T_x$-H and $Ti_3C_2T_x$-DMSO-H as a function of solution pH. (C_0 = 100 mg l^{-1}, m/V = 0.4 g l^{-1}.)

3.4. Adsorption isotherms

The adsorption isotherm experiments were conducted to assess the effect of Th^{IV} equilibrium concentration on the adsorption behavior of the MXenes. As shown in Fig. 5, over the initial concentration range of 5–150 mg l^{-1}, the obtained maximum experimental adsorption capacities (Q_{max}) of Th^{IV} for $Ti_3C_2T_x$-D, $Ti_3C_2T_x$-H and $Ti_3C_2T_x$-DMSO-H at pH 3.4 were 46, 126 and 162 mg g^{-1}, while the corresponding Q_{max} at pH 3.0 were 17, 86 and 112 mg g^{-1}, respectively. $Ti_3C_2T_x$-DMSO-H had the best Th^{IV} enrichment performance among the three MXene samples, which is attributed to the most available active adsorption sites stemming from its largest interlayer space.

To further evaluate the adsorption mechanism, Langmuir and Freundlich isotherm models were used to fit the experimental data. The former mainly describes monolayer adsorption and the latter is suitable for the interpretation of multilayer adsorption. The equations of the two models are expressed as follows in order:

$$C_e/Q_e = 1/Q_m K_L + C_e/Q_m \quad (4)$$

$$\ln Q_e = \ln k_F + (\ln C_e)/n. \quad (5)$$

For the Langmuir model [equation (4)], Q_m is the maximum adsorption capacity (mg g^{-1}) corresponding to a complete monolayer coverage and k_L is a constant indirectly related to the sorption capacity and energy of adsorption (l mg^{-1}), which characterizes the affinity of the adsorbate to the adsorbent. As for the Freundlich model [equation (5)], Q_e (mg g^{-1}) is the equilibrium adsorption amount, k_F and n are the Freundlich constants related to the adsorption capacity and the adsorption intensity, respectively. Based on Fig. 5 and the fitting parameters in Table 2, it is apparent that the Freundlich model

Table 2
Isotherm parameters fitted by the Langmuir and Freundlich models for Th^{IV} adsorption onto $Ti_3C_2T_x$-D, $Ti_3C_2T_x$-H and $Ti_3C_2T_x$-DMSO-H.

	Langmuir model			Freundlich model		
	q_m (mg g^{-1})	k_L (ml mg^{-1})	R^2	k_F (mg g^{-1})	n	R^2
$Ti_3C_2T_x$-D pH 3.4	40.8	0.0367	0.714	3.20	1.95	0.868
$Ti_3C_2T_x$-H pH 3.4	126.4	0.173	0.985	29.5	3.01	0.980
$Ti_3C_2T_x$-DMSO-H pH 3.4	157.7	0.178	0.971	43.3	3.5	0.988
$Ti_3C_2T_x$-D pH 3.0	22.3	0.0192	0.720	1.89	2.35	0.870
$Ti_3C_2T_x$-H pH 3.0	85.7	0.181	0.989	31.2	4.79	0.997
$Ti_3C_2T_x$-DMSO-H pH 3.0	110.7	0.307	0.990	46.7	5.31	0.995

could better describe the adsorption process of Th^{IV} on the three MXene samples. Because the fitting of pH 3.0 and pH 3.4 led to similar results, we concluded that the heterogeneous adsorption of Th^{IV} by $Ti_3C_2T_x$ was a pH-independent intrinsic characteristic. The heterogeneous adsorption mechanism could be explained by the various termination groups (–OH, –O and –F) and unique multilayer structures of $Ti_3C_2T_x$. It was also noted that $Ti_3C_2T_x$-H and $Ti_3C_2T_x$-DMSO-H had larger values of parameter n than $Ti_3C_2T_x$-D, implying a more favorable adsorption of Th^{IV} by the hydrated and intercalated MXene.

3.5. Effect of temperature and thermodynamic study

The adsorption of Th^{IV} onto the MXene samples was carried out at 280, 290, 300 and 310 K to investigate the effect of temperature. The uptake capacities of $Ti_3C_2T_x$-D, $Ti_3C_2T_x$-H and $Ti_3C_2T_x$-DMSO-H increased with increasing temperature [Fig. 6(*a*)], suggesting that a higher temperature is favorable for the adsorption of Th^{IV} by $Ti_3C_2T_x$. Thermodynamic evaluation of an adsorption process is necessary to conclude whether the process is spontaneous or not. The Gibb's free energy change (ΔG^0, kJ mol^{-1}), enthalpy change (ΔH^0, kJ mol^{-1}) and entropy change (ΔS^0, J mol^{-1} K^{-1}) can be calculated by equations (6) and (7):

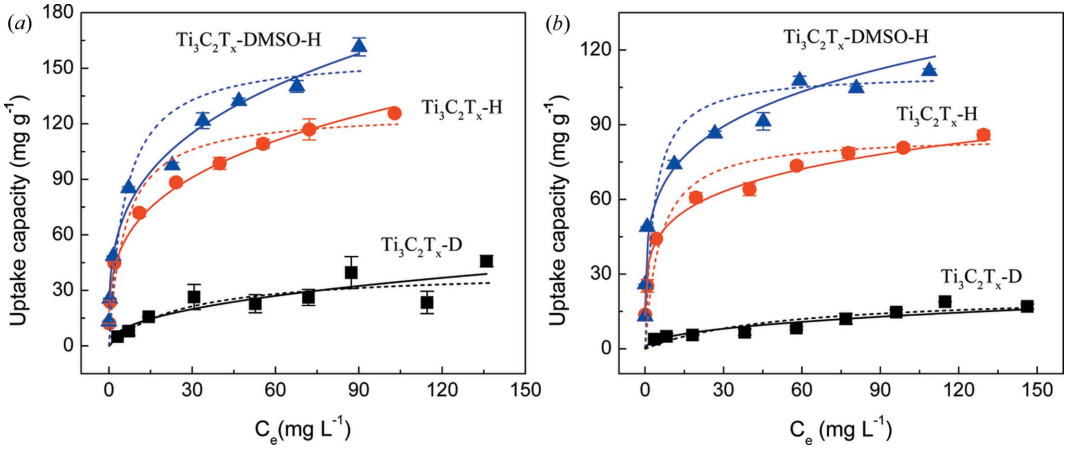

Figure 5
Adsorption isotherms of Th^{IV} uptake onto $Ti_3C_2T_x$-D, $Ti_3C_2T_x$-H and $Ti_3C_2T_x$-DMSO-H. (*a*) pH 3.4 ± 0.1; (*b*) pH 3.0 ± 0.1; solid line: fitted by Freundlich model; dashed line: fitted by Langmuir model.

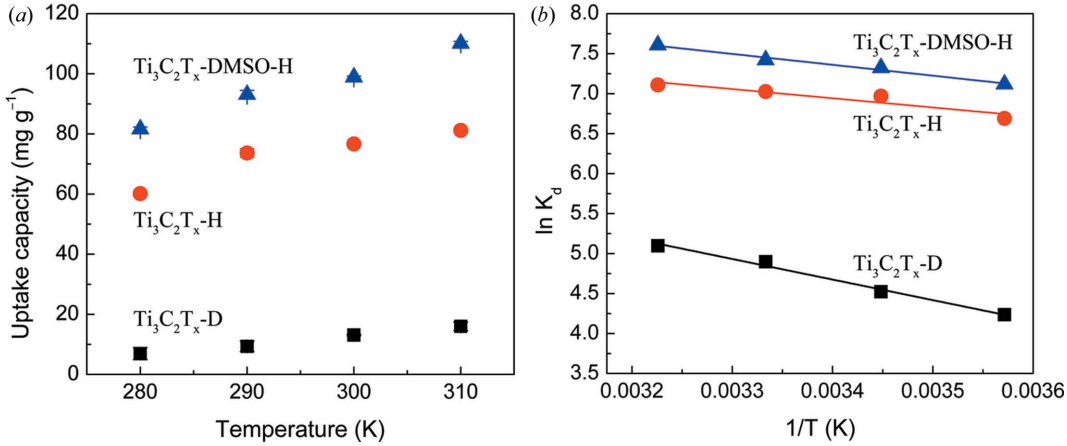

Figure 6
(*a*) Effect of temperature on the adsorption of Th^{IV} by $Ti_3C_2T_x$-D, $Ti_3C_2T_x$-H and $Ti_3C_2T_x$-DMSO-H. (C_0 = 100 mg l^{-1}, pH = 3.0±0.1, m/V = 0.4 g l^{-1}); (*b*) Van't Hoff equation plots for the adsorption of Th^{IV} onto $Ti_3C_2T_x$-D, $Ti_3C_2T_x$-H and $Ti_3C_2T_x$-DMSO-H.

$$\Delta G^0 = -RT \ln K_d \quad (6)$$

$$\Delta G^0 = \Delta H^0 - T\Delta S^0 \quad (7)$$

where R is the universal gas constant (8.314 J mol^{-1} K^{-1}), T is absolute temperature (K) and K_d represents the distribution coefficient (ml g^{-1}). Combining equations (6) and (7), ΔH^0 and ΔS^0 can be determined from the linear relationship of $\ln K_d$ versus $1/T$, described as follows:

$$\ln K_d = \Delta S^0/R - \Delta H^0/RT. \quad (8)$$

Fig. 6(*b*) shows the above linear plots and Table 3 lists the thermodynamic parameters calculated from the fitting lines. ΔG^0 is negative at all the conditions applied, confirming that the adsorption of Th^{IV} by $Ti_3C_2T_x$ is spontaneous. $Ti_3C_2T_x$-DMSO-H has the most negative ΔG^0 among the three MXene samples, which reflects the thermodynamically favorable nature of the hydrated intercalated MXene for Th^{IV} adsorption. $\Delta H^0 > 0$ indicates that the adsorption is an endothermic process. $Ti_3C_2T_x$-D has a larger ΔH^0 than the other two samples, which might be related to the hydration/dehydration states of MXene. The positive value of ΔS^0 suggests the increased randomness at the adsorbent/adsorbate interface during the adsorption. Additionally, compared with the thermodynamic data of previously studied hydrated Ti_2CT_x (Li *et al.*, 2019), $Ti_3C_2T_x$-H renders a lower ΔH^0 and ΔS^0, which indicates that the affinity of $Ti_3C_2T_x$ to Th^{IV} is not as strong as that of Ti_2CT_x, although the two MXenes have similar surface termination and layer structure.

Table 3
Fitting results of thermodynamic parameters for Th^{IV} adsorption onto $Ti_3C_2T_x$-D, $Ti_3C_2T_x$-H and $Ti_3C_2T_x$-DMSO-H.

	ΔH (kJ mol^{-1})	ΔS (J mol^{-1} K^{-1})	ΔG (kJ mol^{-1})			
			280 K	290 K	300 K	310 K
$Ti_3C_2T_x$-D	21.39	111.6	−9.86	−10.97	−12.09	−13.21
$Ti_3C_2T_x$-H	9.58	90.3	−15.7	−16.61	−17.51	−18.41
$Ti_3C_2T_x$-DMSO-H	11.30	99.6	−16.59	−17.58	−18.58	−19.58

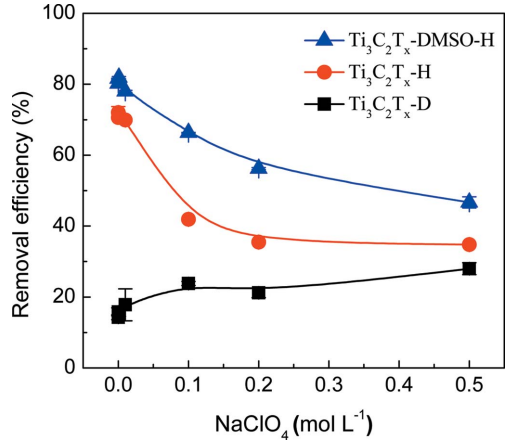

Figure 7
Effect of ionic strength towards Th^{IV} adsorption onto $Ti_3C_2T_x$-D, $Ti_3C_2T_x$-H and $Ti_3C_2T_x$-DMSO-H. (C_0 = 40 mg l^{-1}, pH = 3.4±0.1, m/V = 0.4 g l^{-1}.)

3.6. Effect of ionic strength and selectivity test

Particular attention was also paid in this study to Th^{IV} adsorption under various ionic strengths and competing cations to evaluate the potential of $Ti_3C_2T_x$ in practical applications of radionuclide separation and thorium purification.

As can be seen in Fig. 7, the removal efficiency of Th^{IV} by the hydrated MXenes decreased with the increase in ionic strength, which reflected that the adsorption process might be controlled by the ion exchange mechanism. Nevertheless, $Ti_3C_2T_x$-DMSO-H still exhibited good Th^{IV} uptake performance at the medium ionic strength conditions. The K_d extracted from Fig. 7 was found to be larger than 5000 ml g^{-1} when the ionic strength was $\leq$0.1 mol l^{-1}, confirming $Ti_3C_2T_x$-DMSO-H is an excellent adsorbent for Th^{IV} removal from common wastewater. It is interesting that the removal efficiency of $Ti_3C_2T_x$-D increased with the increase in ionic strength, which is contrary to the behavior of the hydrated $Ti_3C_2T_x$ MXenes. A reasonable explanation is that the presence of a high concentration of Na^+ in aqueous solution may activate the dried $Ti_3C_2T_x$, leading to the intercalation of hydrated ions at the edge of nano-lamellar MXene, thereby increasing the adsorption sites for Th^{IV}.

To evaluate the ion selectivity of the MXene adsorbents, a competing adsorption experiment was also performed in a mixed solution containing Th^{IV} and nine other metal cations. The initial concentration of each metal ion was 0.5 mmol l^{-1}. As shown in Fig. 8(*a*), $Ti_3C_2T_x$-D had almost no selectivity because the adsorption performance of Th^{IV} (mmol g^{-1}) was comparable with other metal ions. The Th^{IV} uptake capacities at pH 3.0 for $Ti_3C_2T_x$-H and $Ti_3C_2T_x$-DMSO-H were 0.33 and 0.40 mmol g^{-1}, and at pH 3.4 they were 0.39 and 0.45 mmol g^{-1}, respectively, whereas the uptake capacities for other competing ions were as low as less than 0.07 mmol g^{-1}. The selectivity coefficients, which we defined as the ratio of K_d of Th^{IV} to that of the competing ions, were calculated to be larger than 8.3 and 9.4 for $Ti_3C_2T_x$-H and $Ti_3C_2T_x$-DMSO-H at pH 3.0, respectively, suggesting a desirable selectivity of the hydrated and intercalated $Ti_3C_2T_x$ for Th^{IV}.

3.7. Adsorption mechanism

To clarify the underlying adsorption mechanism, the MXene samples loaded with Th^{IV} were vacuum dried and then subjected to SEM, EDS and XRD characterization. SEM images in Figs. 2(*d*)–2(*f*) indicated that the multilayer structures of $Ti_3C_2T_x$ MXene were well retained after adsorption. EDS results in Figs. 2(*g*)–2(*i*) clearly confirmed that the content of Th in the MXene samples increased rapidly with the expansion of $Ti_3C_2T_x$ interlayer space, which is consistent with the results of batch adsorption experiments. The comparison of XRD patterns can reflect the interaction behavior between layered materials and guest ions. According to Fig. 9(*a*) and Fig. S3, the (002) peak position of $Ti_3C_2T_x$-D remained unchanged after the adsorption, suggesting that no

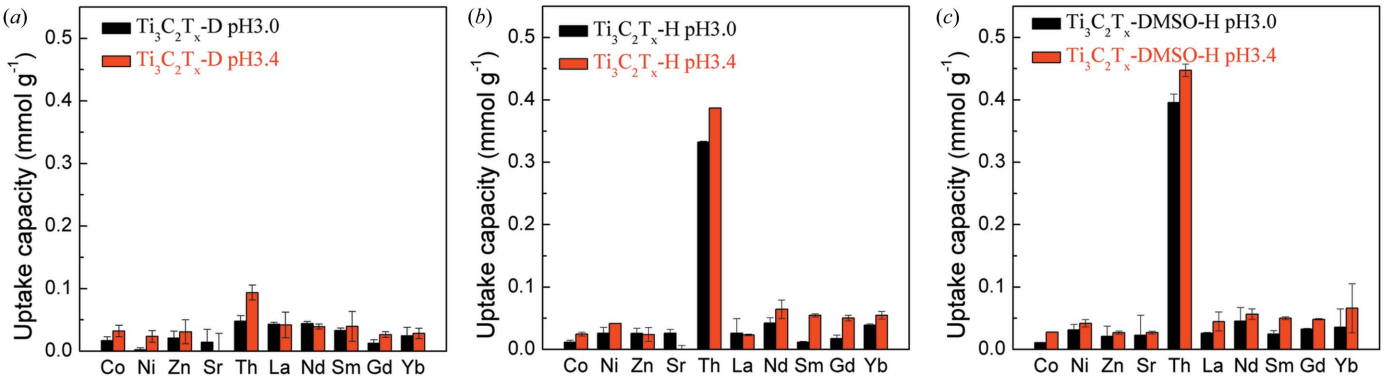

Figure 8
Effect of competing metal cations on the removal of Th^{IV} by $Ti_3C_2T_x$-D (*a*), $Ti_3C_2T_x$-H (*b*) and $Ti_3C_2T_x$-DMSO-H (*c*) at pH 3.0 and 3.4. (C_0 = 0.5 mmol l^{-1} for all cations, m/V = 0.4 g l^{-1}.)

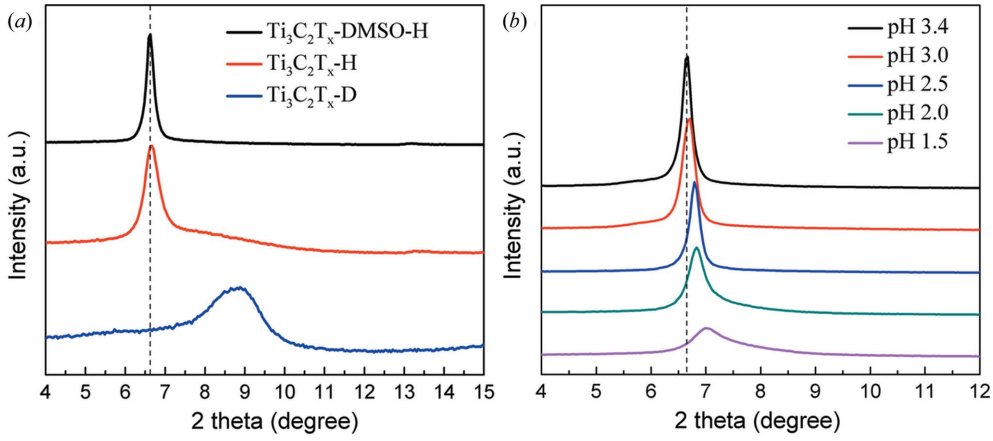

Figure 9
(*a*) XRD patterns of the Th-loaded MXene samples at pH 3.4; (*b*) XRD patterns of the Th-loaded $Ti_3C_2T_x$-DMSO-H at different solution pH.

hydrated Th^{IV} ions entered the interlayers, and the uptake of Th^{IV} only occurred on the exterior surface of MXene. For hydrated MXenes including $Ti_3C_2T_x$-DMSO-H and $Ti_3C_2T_x$-H, the (002) peak shifted to 6.6° after the adsorption, revealing the successful intercalation of Th^{IV} in these samples. Since the solution pH had a slight decrease after the adsorption, we attribute the intercalation to the replacement of hydrated H^+ by Th^{IV} in the interlayers of MXene, namely, there may be an ion exchange reaction. An estimation of the size of intercalated ions was carried out by calculating the enlarged interlayer space (1/2 Δ*c*-LP) between Th-loaded $Ti_3C_2T_x$-DMSO-H/$Ti_3C_2T_x$-H and $Ti_3C_2T_x$-D samples. The dimension of intercalated Th^{IV} was calculated to be about 3.4 Å, which is smaller than the previously reported size of intercalated uranyl ions (3.9 Å) (Wang *et al.*, 2017). This difference in size is reasonable because the hydrated thorium ion has a spherical configuration while the hydrated uranyl ion prefers equatorial plane coordination. Fig. 9(*b*) shows the effect of pH on the *c*-LP of Th-loaded $Ti_3C_2T_x$-DMSO-H. As the reaction pH decreased, the *c*-LP of MXene decreased from 26.7 to 25.1 Å, and the intensity of the (002) peak was also significantly weakened. This result shows that the interlayer adsorption amount and the chemical species of Th^{IV} under different pH together determine its intercalation behavior inside MXene interlayers.

The EXAFS technique can probe the local environment around Th atoms (Shi *et al.*, 2014), and therefore provide important information for understanding the microscopic mechanism of Th^{IV} adsorption on the $Ti_3C_2T_x$ MXene. The Th L_3 edge k^3-weighted EXAFS spectra of the Th-loaded hydrated MXenes and the references are shown on the left side of Fig. 10. The EXAFS data for the $Ti_3C_2T_x$-D sample are not available due to the poor quality of the spectrum caused by low Th^{IV} adsorption capacity. The oscillation periods of $Ti_3C_2T_x$-DMSO-H at pH 2.0 are consistent with that of Th^{IV} aqueous solution, but are significantly different from $Th(NO_3)_4{\cdot}5H_2O$, implying the presence of highly hydrated Th^{IV} ions in the adsorbent and there were no coordinated nitrates around Th atoms. The amplitudes at $k > 8.5$ Å become lower under higher pH (*e.g.* pH 3.0 and 3.4), which reflects a lack of long-range order of Th^{IV} in the MXene interlayers. Fig. 10 (right side) represents the associated Fourier transform (FT) spectra in *R* space, and the fitting results are shown in Table 4. The FT spectra exhibit a strong peak at around 2 Å (without phase-shift correction), which can be ascribed to the first oxygen coordination shell surrounding the Th^{IV} atom. The average Th—O distance was fitted as 2.46 Å with a CN of 10.7 for Th^{IV} aqueous solution, which is in good agreement with the literature (Dähn *et al.*, 2002; Rothe *et al.*, 2002; Zhang *et al.*, 2017). The sample of $Ti_3C_2T_x$-DMSO-H at pH 2.0 had 10.1

Table 4
Fitting parameters extracted from least-squares fitting analysis of EXAFS spectra.

CN, coordination number; R, radial distance; ΔE, energy shift relative to the calculated Fermi level; σ^2, Debye–Waller factor; R factor, goodness-of-fit indicator.

Sample	Path	CN	R (Å)	ΔE (eV)	σ^2 (Å^2)	R factor
$Th(NO_3)_4{\cdot}5H_2O$	Th–O	11.0†	2.52 ± 0.02	5.32 ± 1.39	0.009	0.016
	Th–N	4.0†	3.08 ± 0.04		0.007	
Th^{4+} (aq)	Th–O	10.7 ± 0.7	2.46 ± 0.01	7.67 ± 0.58	0.009	0.009
$Ti_3C_2T_x$-DMSO-H pH 2.0	Th–O	10.1 ± 0.8	2.46 ± 0.01	6.75 ± 0.65	0.010	0.011
$Ti_3C_2T_x$-DMSO-H pH 3.0	Th–O	9.5 ± 0.8	2.43 ± 0.01	5.51 ± 0.69	0.013	0.010
$Ti_3C_2T_x$-DMSO-H pH 3.4	Th–O	8.9 ± 0.8	2.43 ± 0.01	5.09 ± 0.77	0.013	0.011
$Ti_3C_2T_x$-H pH 3.4	Th–O	9.0 ± 0.7	2.44 ± 0.01	5.39 ± 0.64	0.012	0.017

† Fixed during fitting.

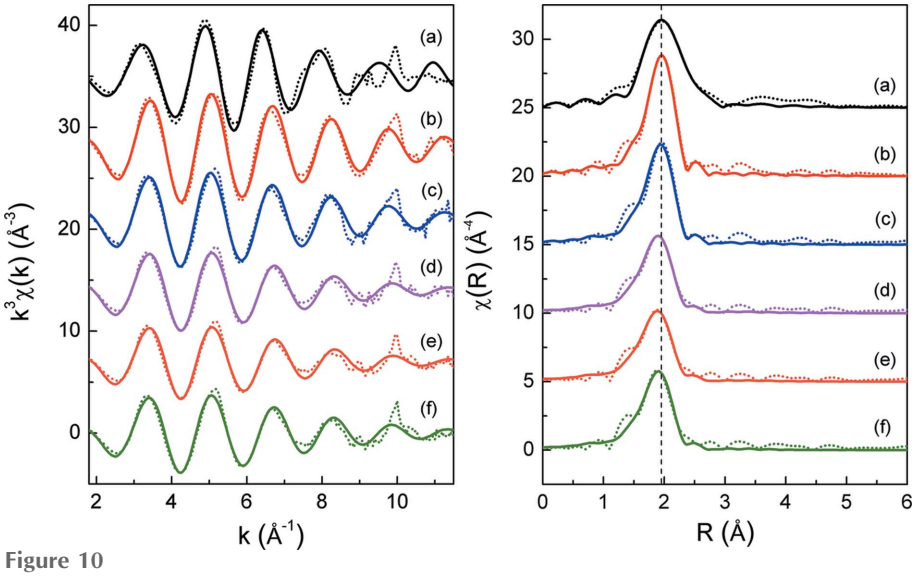

Figure 10
Left: Th L_3 edge k_3-weighted EXAFS spectra (dotted lines) and the best fits (solid lines) for the MXene samples under different solution pH. Right: corresponding non-phase-shift-corrected Fourier transforms. (*a*) $Th(NO_3)_4{\cdot}5H_2O$ reference; (*b*) aqueous Th^{IV} solution; (*c*) $Ti_3C_2T_x$-DMSO-H pH 2.0; (*d*) $Ti_3C_2T_x$-DMSO-H pH 3.0; (*e*) $Ti_3C_2T_x$-DMSO-H pH 3.4; (*f*) $Ti_3C_2T_x$-H pH 3.4.

oxygen atoms at 2.46 Å. Although the CN is slightly reduced due to the confinement of the MXene interlayer, this result is similar to that of Th^{IV} aqueous solution, which indicates that electrostatic interaction is dominant during the adsorption process under low pH conditions. When the solution pH increased to 3.0 and 3.4, the Th—O distance shifted to 2.43 Å, while concomitantly the CN decreased to 9.5 and 8.9, respectively. It has been reported that the compact Th—O bond at 2.40–2.42 Å and the CN of 8.0–9.0 usually correspond to the formation of stable inner-sphere complexes for Th^{IV} (Seco *et al.*, 2009; Zhang *et al.*, 2017). Therefore, our fitting results indicate that the contribution of surface complexation to Th^{IV} adsorption on $Ti_3C_2T_x$ cannot be ignored at such pH conditions. Additionally, the fitting parameters of $Ti_3C_2T_x$-H are very close to that of $Ti_3C_2T_x$-DMSO-H at pH 3.4, reflecting that the different intercalated guest in this study (water or a mixture of water and DMSO molecules) will not significantly affect the underlying adsorption mechanism. The FTIR spectra in Fig. 11 provide further information to support the above conclusion. After Th^{IV} uptake, the intensity of the absorption peak at 649 cm^{-1} decreased and the absorption peak at 561 cm^{-1} clearly shifted to 568 cm^{-1} for both hydrated MXenes, whereas the absorption peaks for $Ti_3C_2T_x$-D were almost unchanged. The absorption bands in the range of 560–650 cm^{-1} can be ascribed to the Ti–O interaction of $Ti_3C_2T_x$ MXene (Peng *et al.*, 2014). The changes of FTIR spectra apparently demonstrate the presence of strong affinities between Ti–O and Th^{IV} ions in $Ti_3C_2T_x$-H and $Ti_3C_2T_x$-DMSO-H. Combined with the fact that the ionic strength could influence the uptake capacity of MXene, we conclude that under higher pH conditions (pH > 3.0), the adsorption of Th^{IV} on hydrated $Ti_3C_2T_x$ is jointly determined by inner-sphere complexation and electrostatic interaction.

4. Conclusion

In summary, this work systemically studied the adsorption behavior of Th^{IV} by dry, hydrated and intercalated $Ti_3C_2T_x$ MXene samples. Because of the full utilization of the active sites inside the interlayers, the intercalation adsorption of Th^{IV} was dominant for the hydrated MXenes, while only external surface adsorption was available for the dry MXene, so $Ti_3C_2T_x$-DMSO-H and $Ti_3C_2T_x$-H exhibited higher uptake capacities and slower kinetics. Our work demonstrated that the elimination of Th^{IV} by $Ti_3C_2T_x$ was a spontaneous endothermic reaction which followed a heterogeneous adsorption model. $Ti_3C_2T_x$ showed a lower affinity for binding Th^{IV}

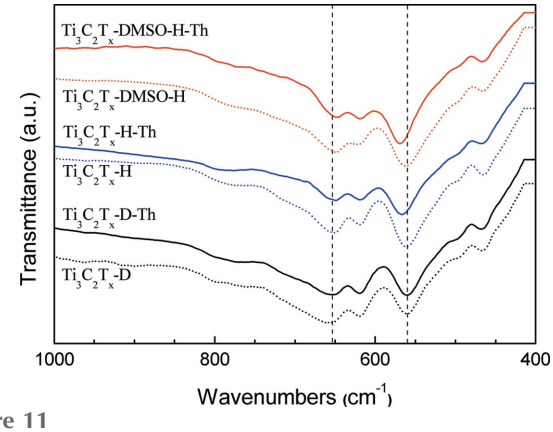

Figure 11
FTIR spectra of the MXene samples before (dotted lines) and after (solid lines) Th^{IV} adsorption.

compared with its titanium-based analog Ti_2CT_x, and the adsorption process could be influenced by the ionic strength. Nevertheless, $Ti_3C_2T_x$-DMSO-H still exhibited considerable removal capacity and desirable selectivity for Th^{IV} at moderate concentration of ionic strength and with competing cations, reflecting its application potential in the purification of thorium-containing radioactive wastewater. Additionally, by analyzing the coordination environment and adsorption sites, we confirmed that the adsorption of Th^{IV} on the hydrated $Ti_3C_2T_x$ MXenes was determined by a combination of electrostatic interaction and surface complexation. These findings can greatly enrich our understanding of the microscopic interactions between MXenes and actinide ions.

Acknowledgements

We are grateful to the staff of Beijing Synchrotron Radiation Facility for the EXAFS measurement.

Funding information

This work was supported by the National Science Fund for Distinguished Young Scholars (grant No. 21925603), the National Natural Science Foundation of China (grant Nos. 22176190, U20B2019, 21906020 and 11875004) and Youth Innovation Promotion Association CAS (2021010).

References

Abbasizadeh, S., Keshtkar, A. R. & Mousavian, M. A. (2013). *Chem. Eng. J.* **220**, 161–171.
Alahabadi, A., Singh, P., Raizada, P., Anastopoulos, I., Sivamani, S., Dotto, G. L., Landarani, M., Ivanets, A., Kyzas, G. Z. & Hosseini-Bandegharaei, A. (2020). *Colloids Surf. A Physicochem. Eng. Asp.* **607**, 125516.
Bai, Z. Q., Li, Z. J., Wang, C. Z., Yuan, L. Y., Liu, Z. R., Zhang, J., Zheng, L. R., Zhao, Y. L., Chai, Z. F. & Shi, W. Q. (2014). *RSC Adv.* **4**, 3340–3347.
Chen, C. L. & Wang, X. K. (2007). *Appl. Geochem.* **22**, 436–445.
Chen, J. Y., Huang, Q., Huang, H. Y., Mao, L. C., Liu, M. Y., Zhang, X. Y. & Wei, Y. (2020). *Nanoscale*, **12**, 3574–3592.
Dähn, R., Scheidegger, A. M., Manceau, A., Curti, E., Baeyens, B., Bradbury, M. H. & Chateigner, D. (2002). *J. Colloid Interface Sci.* **249**, 8–21.
Esen Erden, K. & Donat, R. (2017). *Radiochim. Acta*, **105**, 187–196.
Fralova, L., Lefèvre, G., Madé, B., Marsac, R., Thory, E. & Dagnelie, R. V. H. (2021). *Appl. Geochem.* **127**, 104859.
Huang, H. Z., Sha, X. F., Cui, Y., Sun, S. Y., Huang, H. Y., He, Z. Y., Liu, M. Y., Zhou, N. G., Zhang, X. Y. & Wei, Y. (2020). *J. Colloid Interface Sci.* **567**, 190–201.
Ihsanullah, I. (2020). *Chem. Eng. J.* **388**, 124340.
Jun, B. M., Jang, M., Park, C. M., Han, J. & Yoon, Y. (2020). *Nucl. Eng. Technol.* **52**, 1201–1207.
Jun, B. M., Park, C. M., Heo, J. & Yoon, Y. (2020). *J. Environ. Manage.* **256**, 109940.
Kaygun, A. K. & Akyil, S. (2007). *J. Hazard. Mater.* **147**, 357–362.
Khan, A. R., Husnain, S. M., Shahzad, F., Mujtaba-ul-Hassan, S., Mehmood, M., Ahmad, J., Mehran, M. T. & Rahman, S. (2019). *Dalton Trans.* **48**, 11803–11812.
Lebed, P. J., de Souza, K., Bilodeau, F., Larivière, D. & Kleitz, F. (2011). *Chem. Commun.* **47**, 11525–11527.
Li, F. H., Yang, Z., Weng, H. Q., Chen, G., Lin, M. Z. & Zhao, C. (2018). *Chem. Eng. J.* **332**, 340–350.
Li, S. X., Wang, L., Peng, J., Zhai, M. L. & Shi, W. Q. (2019). *Chem. Eng. J.* **366**, 192–199.
Li, X., Li, Q., Linghu, W. S., Shen, R. P., Zhao, B. S., Dong, L. J., Alsaedi, A., Hayat, T., Wang, J. & Liu, J. (2018). *Environ. Technol. Innov.* **11**, 328–338.
Liu, W., Dai, X., Wang, Y. L., Song, L. P., Zhang, L. J., Zhang, D., Xie, J., Chen, L., Diwu, J., Wang, J. Q., Chai, Z. F. & Wang, S. (2019). *Environ. Sci. Technol.* **53**, 332–341.
Magnuson, M. & Näslund, L.-Å. (2020). *Phys. Rev. Res.* **2**, 033516.
Misaelides, P., Godelitsas, A., Filippidis, A., Charistos, D. & Anousis, I. (1995). *Sci. Total Environ.* **173–174**, 237–246.
Moghaddam, Z. S., Kaykhaii, M., Khajeh, M. & Oveisi, A. R. (2018). *Spectrochim. Acta A Mol. Biomol. Spectrosc.* **194**, 76–82.
Mu, W. J., Du, S. Z., Li, X. L., Yu, Q. H., Wei, H. Y., Yang, Y. C. & Peng, S. M. (2019). *Chem. Eng. J.* **358**, 283–290.
Mu, W. J., Du, S. Z., Yu, Q. H., Li, X. L., Wei, H. Y. & Yang, Y. C. (2018). *Dalton Trans.* **47**, 8375–8381.
Naguib, M., Kurtoglu, M., Presser, V., Lu, J., Niu, J. J., Heon, M., Hultman, L., Gogotsi, Y. & Barsoum, M. W. (2011). *Adv. Mater.* **23**, 4248–4253.
Naguib, M., Mashtalir, O., Carle, J., Presser, V., Lu, J., Hultman, L., Gogotsi, Y. & Barsoum, M. W. (2012). *ACS Nano*, **6**, 1322–1331.
Naslund, L. A., Mikkela, M. H., Kokkonen, E. & Magnuson, M. (2021). *2D Mater.* **8**, 045026.
Peng, Q. M., Guo, J. X., Zhang, Q. R., Xiang, J. Y., Liu, B. Z., Zhou, A. G., Liu, R. P. & Tian, Y. J. (2014). *J. Am. Chem. Soc.* **136**, 4113–4116.
Rao, T. P., Metilda, P. & Gladis, J. M. (2006). *Talanta*, **68**, 1047–1064.
Rasool, K., Pandey, R. P., Rasheed, P. A., Buczek, S., Gogotsi, Y. & Mahmoud, K. A. (2019). *Mater. Today*, **30**, 80–102.
Ravel, B. & Newville, M. (2005). *J. Synchrotron Rad.* **12**, 537–541.
Reiller, P., Casanova, F. & Moulin, V. (2005). *Environ. Sci. Technol.* **39**, 1641–1648.
Rojo, I., Seco, F., Rovira, M., Giménez, J., Cervantes, G., Martí, V. & de Pablo, J. (2009). *J. Nucl. Mater.* **385**, 474–478.
Rothe, J., Denecke, M. A., Neck, V., Müller, R. & Kim, J. I. (2002). *Inorg. Chem.* **41**, 249–258.
Seco, F., Hennig, C., de Pablo, J., Rovira, M., Rojo, I., Martí, V., Giménez, J., Duro, L., Grivé, M. & Bruno, J. (2009). *Environ. Sci. Technol.* **43**, 2825–2830.
Shahzad, A., Moztahida, M., Tahir, K., Kim, B., Jeon, H., Ghani, A. A., Maile, N., Jang, J. & Lee, D. S. (2020). *J. Nucl. Mater.* **539**, 152277.
Sheng, G. D., Hu, J. & Wang, X. K. (2008). *Appl. Radiat. Isot.* **66**, 1313–1320.
Shi, W. Q., Yuan, L. Y., Wang, C. Z., Wang, L., Mei, L., Xiao, C. L., Zhang, L., Li, Z. J., Zhao, Y. L. & Chai, Z. F. (2014). *Adv. Mater.* **26**, 7807–7848.
Tan, X. L., Wang, X. K., Chen, C. L. & Sun, A. H. (2007). *Appl. Radiat. Isot.* **65**, 375–381.
VahidMohammadi, A., Rosen, J. & Gogotsi, Y. (2021). *Science*, **372**, eabf1581.
Wang, L., Li, Z. J., Wu, Q. Y., Huang, Z. W., Yuan, L. Y., Chai, Z. F. & Shi, W. Q. (2020). *Environ. Sci.: Nano*, **7**, 724–752.
Wang, L., Song, H., Yuan, L., Li, Z., Zhang, P., Gibson, J. K., Zheng, L., Wang, H., Chai, Z. & Shi, W. (2019). *Environ. Sci. Technol.* **53**, 3739–3747.
Wang, L., Song, H., Yuan, L. Y., Li, Z. J., Zhang, Y. J., Gibson, J. K., Zheng, L. R., Chai, Z. F. & Shi, W. Q. (2018). *Environ. Sci. Technol.* **52**, 10748–10756.
Wang, L., Tao, W. Q., Yuan, L. Y., Liu, Z. R., Huang, Q., Chai, Z. F., Gibson, J. K. & Shi, W. Q. (2017). *Chem. Commun.* **53**, 12084–12087.
Wang, L., Yuan, L. Y., Chen, K., Zhang, Y. J., Deng, Q. H., Du, S. Y., Huang, Q., Zheng, L. R., Zhang, J., Chai, Z. F., Barsoum, M. W., Wang, X. K. & Shi, W. Q. (2016). *ACS Appl. Mater. Interfaces*, **8**, 16396–16403.

Wang, S. Y., Wang, L., Li, Z. J., Zhang, P. C., Du, K., Yuan, L. Y., Ning, S. Y., Wei, Y. Z. & Shi, W. Q. (2021). *J. Hazard. Mater.* **408**, 124949.
Wang, Y. L., Liu, W., Bai, Z. L., Zheng, T., Silver, M. A., Li, Y. X., Wang, Y. X., Wang, X., Diwu, J., Chai, Z. F. & Wang, S. (2018). *Angew. Chem. Int. Ed.* **57**, 5783–5787.
Wang, Z. J., Brown, A. T., Tan, K., Chabal, Y. J. & Balkus, K. J. (2018). *J. Am. Chem. Soc.* **140**, 14735–14739.
Wu, H. Y., Qiang, S. R., Fan, Q. H., Zhao, X. L., Liu, P., Li, P., Liang, J. J. & Wu, W. S. (2018). *Appl. Clay Sci.* **152**, 295–302.
Xu, L., Xu, C., Bao, H. L., Spanopoulos, I., Ke, W. J., Dong, X., Xiao, C. L. & Kanatzidis, M. G. (2021). *ACS Appl. Mater. Interfaces*, **13**, 37308–37315.
Ying, Y. L., Liu, Y., Wang, X. Y., Mao, Y. Y., Cao, W., Hu, P. & Peng, X. S. (2015). *ACS Appl. Mater. Interfaces*, **7**, 1795–1803.
Yuan, D. Z., Zhang, S. A., Xiang, Z. H., He, Y., Wang, Y., Liu, Y., Zhao, X. H., Zhou, X. Y. & Zhang, Q. H. (2019). *ACS Appl. Mater. Interfaces*, **11**, 24512–24522.
Yuan, L. Y., Bai, Z. Q., Zhao, R., Liu, Y. L., Li, Z. J., Chu, S. Q., Zheng, L. R., Zhang, J., Zhao, Y. L., Chai, Z. F. & Shi, W. Q. (2014). *ACS Appl. Mater. Interfaces*, **6**, 4786–4796.
Yusan, S., Bampaiti, A., Erenturk, S., Noli, F., Aslani, M. A. A. & Aytas, S. (2016). *Radiochim. Acta*, **104**, 635–647.
Zhang, F., Ma, K. Q., Li, Y., Ran, Q., Yao, C. Y., Yang, C. T., Yu, H. Z., Hu, S. & Peng, S. M. (2020). *Chem. Eng. J.* **392**, 123717.
Zhang, H. X., Wang, X. Y., Liang, H. H., Tan, T. S. & Wu, W. S. (2016). *Appl. Clay Sci.* **127**, 35–43.
Zhang, N., Yuan, L. Y., Guo, W. L., Luo, S. Z., Chai, Z. F. & Shi, W. Q. (2017). *ACS Appl. Mater. Interfaces*, **9**, 25216–25224.
Zhang, P., Wang, L., Du, K., Wang, S., Huang, Z., Yuan, L., Li, Z., Wang, H., Zheng, L., Chai, Z. & Shi, W. (2020). *J. Hazard. Mater.* **396**, 122731.
Zhao, D. L. (2008). *Appl. Clay Sci.* **41**, 17–23.
Zhou, W. N., Wang, H. Q., Hou, S. Y. & Wang, S. (2021). *J. Radioanal. Nucl. Chem.* **329**, 253–263.